Ternary wurtzite CaAgBi materials family: A playground for essential and accidental, type-I and type-II Dirac fermions

Cong Chen,[1,2] Shan-Shan Wang,[2] Lei Liu,[3] Zhi-Ming Yu,[2,*] Xian-Lei Sheng,[1,2,†] Ziyu Chen,[1] and Shengyuan A. Yang[2]

[1]*Department of Physics, Key Laboratory of Micro-nano Measurement-Manipulation and Physics (Ministry of Education), Beihang University, Beijing 100191, China*

[2]*Research Laboratory for Quantum Materials, Singapore University of Technology and Design, Singapore 487372, Singapore*

[3]*State Key Laboratory of Integrated Service Networks, Xidian University, Xi'an 710071, China*

(Received 3 July 2017; published 6 September 2017)

Based on their formation mechanisms, Dirac points in three-dimensional systems can be classified as accidental or essential. The former can be further distinguished into type I and type II, depending on whether the Dirac cone spectrum is completely tipped over along a certain direction. Here we predict the coexistence of all three kinds of Dirac points in the low-energy band structure of CaAgBi-family materials with a stuffed wurtzite structure. Two pairs of accidental Dirac points reside on the rotational axis, with one pair being type I and the other pair type II; while another essential Dirac point is pinned at the high symmetry point on the Brillouin zone boundary. Due to broken inversion symmetry, the band degeneracy around accidental Dirac points is completely lifted except along the rotational axis, realizing a kind of birefringent Dirac fermions, which may enable the splitting of chiral carriers at a ballistic p-n junction with a double negative refraction effect. We clarify their symmetry protections, and find both the Dirac cone and Fermi arc topological surface states.

DOI: 10.1103/PhysRevMaterials.1.044201

I. INTRODUCTION

Topological semimetals have been attracting tremendous interest in current research [1–4], partly because they offer a convenient platform to explore the intriguing physics of high-energy elementary particles. For example, Weyl semimetals possess linearly dispersing twofold-degenerate Weyl points close to Fermi energy [5–11]. Each Weyl point has a definite chirality of ± 1, around which the quasiparticle excitations mimic the relativistic Weyl fermions [12,13]. Two Weyl points with opposite chirality would be unstable towards gap opening when they meet at the same k point, unless there exists additional symmetry protection, such as the case in so-called Dirac semimetals [14], in which stable Dirac points with fourfold degeneracy make it possible to simulate massless Dirac fermions.

Dirac points can be classified as accidental or essential [15] (see Fig. 1). Accidental Dirac points require band inversion (which is in a sense accidental) and are stabilized by certain symmorphic crystalline symmetries such as rotation, so such Dirac points typically reside on high-symmetry lines. Examples include the experimentally confirmed Dirac semimetals Na_3Bi [16,17] and Cd_3As_2 [18–21]. Essential Dirac points do not need band inversion, and their presence is solely determined by certain nonsymmorphic symmetries at high-symmetry points on the boundary of the Brillouin zone (BZ). Examples include the first few proposals such as β-cristobalite BiO_2 [14] and several Bi-containing distorted spinels [22]. Accidental Dirac points can be removed by reverting the band ordering without changing the symmetry, whereas essential Dirac points cannot. In addition, since accidental Dirac points are located at k points with lower symmetry (compared with essential ones), the dispersions around them are less constrained. It is possible to have the Dirac cone completely tipped over along a certain direction [23,24], realizing a so-called type-II Dirac point [25], which has been identified in VAl_3 [25], $PdTe_2$ [26–28], $PtSe_2$ family [29–31], and others [32–34]. Fascinating yet distinct physics have been proposed for type-I and type-II points [35–37], and it has been theoretically argued in the context of Weyl points that when both types coexist in a single hybrid material, even more interesting effects could appear [38,39].

In this work we show that all the above-mentioned three kinds of Dirac points are simultaneously present in the low-energy band structure of CaAgBi-family materials. Two pairs of accidental Dirac points are realized on the k_z axis and are protected by the C_{6v} point group symmetry, with one pair being type I and the other pair type II. Meanwhile, another single essential Dirac point occurs at the A point on the boundary of BZ, as dictated by the nonsymmorphic space group symmetry. The inversion symmetry, preserved in most Dirac semimetals proposed so far, is broken in the CaAgBi-family materials. Consequently, the dispersions around the Dirac points exhibit distinct features. Particularly, the band degeneracy around the accidental Dirac points is lifted due to the broken inversion symmetry (except along the rotational axis), making it possible to split the chiral carriers at a ballistic p-n junction with a double negative refraction effect. We clarify the symmetry protection mechanisms, and find interesting surface-orientation-dependent topological surface states including both the Dirac-cone surface bands and the surface Fermi arcs. This class of hybrid Dirac materials offers a promising platform to explore the intriguing physics of Dirac fermions.

II. METHODOLOGY AND MATERIALS

The first-principle results are based on density-functional theory (DFT) as implemented in Vienna *ab initio* simulation

*zhiming_yu@sutd.edu.sg
†xlsheng@buaa.edu.cn

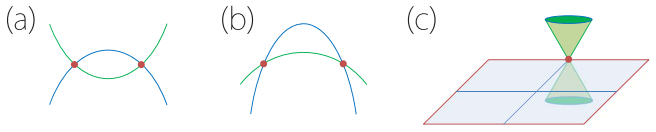

FIG. 1. Three kinds of Dirac points. (a) Type-I and (b) type-II accidental Dirac points. Here each band is twofold degenerate. (c) Essential Dirac point located at high-symmetry point on the Brillouin zone boundary.

package (VASP) [40,41] and with the projector augmented wave (PAW) method [42]. The generalized gradient approximation (GGA) with Perdew-Burke-Ernzerhof (PBE) [43] realization was adopted for the exchange-correlation potential. The plane-wave cutoff energy was taken as 500 eV. The Monkhorst-Pack k-point mesh [44] of size $11 \times 11 \times 8$ was used for Brillouin zone (BZ) sampling. The crystal structures were optimized until the forces on the ions are less than 0.01 eV/Å. From the DFT results, we constructed the maximally localized Wannier functions (MLWF) [45] for Ag-5s and Bi-6p orbitals, and tight-binding model Hamiltonians for bulk and semi-infinite layer were built to investigate the surface states.

In this work, we focus on the CaAgBi-family materials, which take a stuffed wurtzite-type structure, with space group No. 186 ($P6_3mc$) [46], as shown in Fig. 2. The structure may be viewed as a zinc-blende structure compressed along the [111] direction. For the first-principles calculations, we take the experimental lattice parameters [46] $a = b = 4.8113$ Å and $c = 7.8273$ Å for CaAgBi. For other materials, we used their optimized lattice parameteres: for CaAgAs, $a = b = 4.5054$ Å and $c = 7.7114$ Å; for CaAuSb, $a = b = 4.7047$ Å and $c = 7.9182$ Å; for CaAuBi, $a = b = 4.8598$ Å and $c = 7.9142$ Å; for SrAgBi, $a = b = 4.9613$ Å and $c = 8.5778$ Å.

III. ELECTRONIC BAND STRUCTURE

Since members of this family show similar low-energy band features, we shall focus on CaAgBi as a representative in the following discussion. It is found that the low-energy states are mainly from the orbitals of Ag and Bi atoms, which lie in the (110) mirror plane. Notably, the structure does not preserve an inversion center. Besides the (110) mirror plane M_x (here we take [110] as x direction), two other important crystalline symmetries are the threefold rotation C_{3z} and the twofold screw rotation $S_{2z} = \{C_{2z}|00\frac{1}{2}\}$.

Figure 3(a) shows the plot of calculated band structure of CaAgBi with spin-orbit coupling (SOC) included. One observes that the material is a semimetal, and the bands around Fermi level are dominated by the Ag-5s and Bi-6p orbitals. Normally, Ag-5s orbitals have a higher energy than Bi-6p orbitals. However, around Γ point, one observes a band inversion feature with Ag-5s lower than Bi-6p. Importantly, along the k_z axis (Γ-A), the three low-energy bands cross pairwisely and linearly at three discrete points, which we label as D_1, D_2, and D_3, as shown in Fig. 3(b). D_1 and D_2 are on the rotational axis, which are accidental crossing points originated from the band inversion at Γ. In contrast, D_3 is pinned at A point on the BZ boundary, which is an essential crossing point dictated by the space group symmetry. One notes that each of the three crossing bands are twofold degenerate (with SOC) on Γ-A, which is caused by the noncommutativity between S_{2z} (or C_{3z}) and M_x symmetries along this path. Thus each crossing point D_i ($i = 1,2,3$) is of fourfold degeneracy, corresponding to a Dirac point.

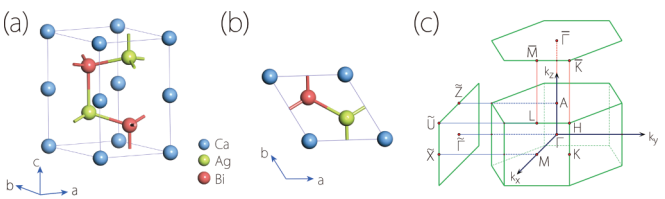

FIG. 2. (a) Side view and (b) top view of the crystal structure of CaAgBi. (c) Corresponding Brillouin zone.

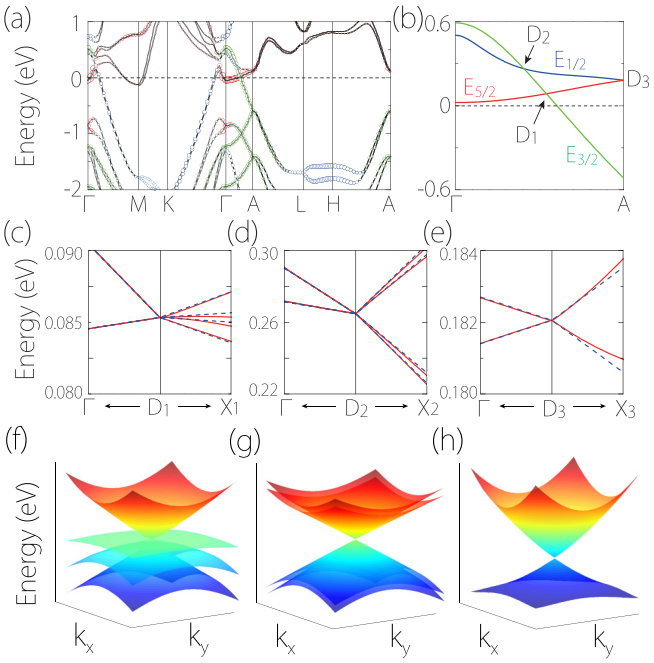

FIG. 3. (a) Band structure of CaAgBi (SOC included). The colored circles indicate the weight of orbital projection onto Ag-s (red), Bi-$p_{x/y}$ (green), and Bi-p_z (blue) orbitals. (b) Enlarged low-energy band structure along Γ-A, showing three Dirac points. (c)–(e) Dispersions around the three Dirac points by first-principles calculations (red solid lines) and $k \cdot p$ model fitting (blue dashed lines). Here D_i-X_i ($i = 1,2,3$) is along the k_x direction perpendicular to the k_z axis. (f)–(h) Three-dimensional view of the three Dirac points on k_x-k_y plane by first-principles calculations.

IV. ACCIDENTAL DIRAC POINTS

Let us first consider the two accidental Dirac points D_1 and D_2. On Γ-A path, the point group symmetry is of C_{6v}, and the three doubly degenerate crossing bands are found to form three *distinct* two-dimensional irreducible representations $E_{1/2}$, $E_{3/2}$, and $E_{5/2}$ of the C_{6v} double group [see Fig. 3(b)]. Therefore, these bands cannot hybridize along this line, and their crossing points are protected and of linear type. The symmetry protection is lost for k points deviating from the rotational axis, hence each crossing should be an

isolated point rather than a line. Another important observation is that while the slopes of the two crossing bands at D_1 have opposite signs, the two bands at D_2 have the same sign. Thus D_1 and D_2 are type-I and type-II Dirac points, respectively.

The dispersions around D_1 and D_2 in the k_x-k_y plane also show interesting features. As shown in Figs. 3(c) and 3(d) and Figs. 3(f) and 3(g), the bands completely split in directions different from the k_z axis, which can be understood by noticing that the twofold band degeneracy on Γ-A cannot be maintained at generic k points in the k_x-k_y plane because such points are not invariant under the rotational symmetries S_{2z} and C_{3z}. This is in contrast to most proposed Dirac semimetals, where the twofold band degeneracy is maintained at any k point due to the presence of inversion symmetry (in combination with time reversal symmetry). Here the splitting of the Dirac cones in the k_x-k_y plane means that there are two species of chiral fermions with different Fermi velocities. This represents a kind of birefringent Dirac fermions, which was previously studied in a few artificial models [47–49]. Our work hence reveals a solid material platform for its realization.

To characterize the low-energy Dirac fermions, we construct the $k \cdot p$ effective models around each Dirac point, subjected to the symmetry constraints [50]. For point D_1, it is at the intersection between $E_{5/2}$ band and $E_{3/2}$ band on Γ-A. Using the four states with such symmetries at D_1 as basis, the Hamiltonian around D_1 up to linear order in $\boldsymbol{q}$ takes the form

$$\mathcal{H}_{D_1} = C_1 q_z + \begin{bmatrix} C_2 q_z & B^* q_+ & iAq_- & 0 \\ Bq_- & -C_2 q_z & 0 & 0 \\ -iAq_+ & 0 & C_2 q_z & -B^* q_- \\ 0 & 0 & -Bq_+ & -C_2 q_z \end{bmatrix}, \tag{1}$$

where the wave-vector $\boldsymbol{q}$ and the energy are measured from D_1, $q_\pm = q_x \pm i q_y$, the model parameters A, C_1, C_2 are real, and B is complex. The first term in Eq. (1) represents a tilt of spectrum. Figure 3(c) shows the fitting of this model to the DFT band structure. Particularly, we find that $|C_2| > |C_1|$, such that the point is of type I with dispersion $\varepsilon = (C_1 \pm C_2) q_z$ along k_z direction. Similarly, we can find the effective model around point D_2, which is at the intersection between $E_{1/2}$ and $E_{3/2}$ bands. We find that the obtained Hamiltonian $\mathcal{H}_{D_2}$ has the same form as $\mathcal{H}_{D_1}$, and only the values of the parameters are different. Most importantly, now $|C_2| < |C_1|$. The dispersion along k_z direction is dominated by the tilt term, so that D_2 is a type-II Dirac point [see Fig. 3(d)].

V. ESSENTIAL DIRAC POINT

Next, we come to the essential Dirac point at A. Its essential character can be argued as follows. The bands along Γ-A can be chosen as S_{2z} eigenstates. Since $(S_{2z})^2 = -e^{-ik_z}$ (the minus sign is from 2π spin rotation, and k_z is measured in unit of $1/c$), the S_{2z} eigenvalues are given by

$$s = \pm i e^{-ik_z/2}. \tag{2}$$

Meanwhile, we have $\{S_{2z}, M_x\} = 0$, so the two states $|s\rangle$ and $M_x|s\rangle$ form a degenerate pair with *opposite* S_{2z} eigenvalues, where $|s\rangle$ denotes an eigenstate of S_{2z} with eigenvalue s. This explicitly demonstrates the twofold band degeneracy along Γ-A, as we claimed before. Note that A is invariant under time reversal operation ($\mathcal{T}$), such that at A, each state $|s\rangle$ has a Kramers degenerate partner $\mathcal{T}|s\rangle$. Since $s = \pm 1$ at point A ($k_z = \pi$), $\mathcal{T}|s\rangle$ shares the same S_{2z} eigenvalue as $|s\rangle$. Consequently, the four states $\{|s\rangle, M_x|s\rangle, \mathcal{T}|s\rangle, \mathcal{T}M_x|s\rangle\}$ at A are linearly independent and must be degenerate with the same energy. Thus the nonsymmorphic space group symmetry necessitates the fourfold degeneracy at A point. The effective model up to linear order in $\boldsymbol{q}$ expanded around D_3 is obtained as

$$\mathcal{H}_{D_3} = v_\perp \sigma_0 \tau_z q_x - v_\perp \sigma_0 \tau_x q_y + v_z \sigma_z \tau_0 q_z. \tag{3}$$

Here $\boldsymbol{q}$ and energy are measured from D_3, σ_i and τ_i are the Pauli matrices, σ_0 and τ_0 are the 2×2 identity matrix, and model parameters $v_\perp$ and v_z correspond to the Fermi velocities. Figure 3(e) shows the fitting of DFT band structure using model (3). Compared with model (1) for the two accidental Dirac points, model (3) has less free parameters due to the additional time reversal symmetry at A. Consequently, the dispersion around D_3 is different from the other two in that: (i) there is no energy tilt term (hence it must be type I); and (ii) the bands in $k_z = \pi$ plane are still twofold degenerate without splitting. Note that this twofold degeneracy is generally lifted for generic k points located neither in the $k_z = \pi$ plane nor on the k_z axis.

VI. SURFACE STATES AND $\mathbb{Z}_2$ INVARIANTS

Band topology and intrinsic anisotropy lead to interesting surface spectra of CaAgBi-family materials, with distinct topological surface states on different crystal surfaces. Here the Dirac points are all residing on k_z axis. They are projected onto the same image point on (001) surface. Since the band is inverted at Γ point in the bulk, we expect to have Dirac-cone type surface states similar to the topological insulator case. In Fig. 4(a) we indeed find such surface states buried in the bulk valence bands. Figure 4(b) shows the constant energy slice above the surface Dirac point, at which the surface states exhibit a left-handed spin helicity, similar to the pattern for strong topological insulators [51,52]. Meanwhile, the Dirac points get projected to different image points on the side surfaces. For (010) surface, we find Fermi arcs connecting a pair of projected Dirac points, as shown in Figs. 4(c) and 4(d) for CaAgAs (for CaAgBi, the arcs are buried in the bulk bands). These Fermi arcs are in fact protected by a bulk $\mathbb{Z}_2$ invariant. Consider the $\mathcal{T}$-invariant planes $k_z = 0$ and $k_z = \pi$. The two planes are fully gapped hence each has a well-defined two-dimensional $\mathbb{Z}_2$ invariant. Due to the broken inversion symmetry, the method of parity counting does not apply here [53]. Instead, we use the Wilson loop method [54–56]. The Wannier center evolution for two representative planes of CaAgBi are shown in Fig. 5 from which we find that $\mathbb{Z}_2 = 1$ for $k_z = 0$ plane, whereas $\mathbb{Z}_2 = 0$ for $k_z = \pi$ plane. Thus a Kramers pair of surface states must exist on the $k_z = 0$ path for the side surfaces, ensuring the presence of a pair of surface Fermi arcs [8,57].

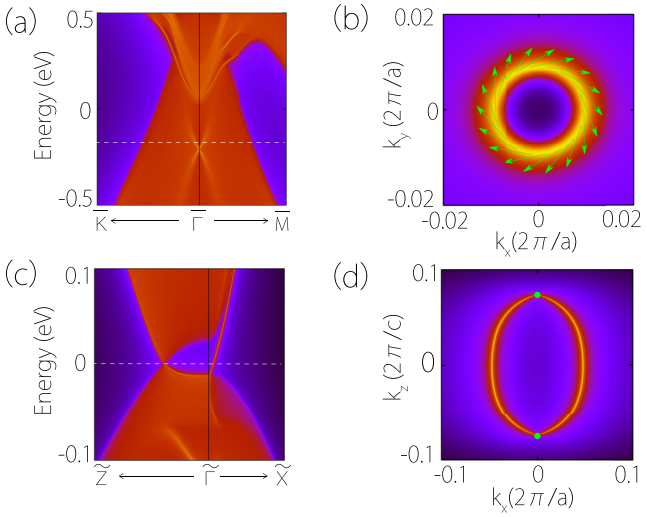

FIG. 4. (a) Projected spectrum on (001) surface for CaAgBi, showing Dirac-cone surface states buried in the bulk valence band. (b) Surface states at −0.18 eV [marked in (a)], showing a left-handed spin-momentum locking. (c) Projected spectrum on (010) surface for CaAgAs, showing (d) surface Fermi arcs connecting a pair of projected Dirac points (green dots).

VII. DISCUSSIONS AND CONCLUSION

We further clarify the distinction between the accidental Dirac points (D_1, D_2) and the essential Dirac point (D_3). The realization of accidental Dirac points requires band inversion. In the current system, this can be characterized by two $\mathbb{Z}_2$ indices ζ_1 and ζ_2. Here

$$\zeta_1 = \mathrm{sgn}(\Delta_{\Gamma,1}\Delta_{A,1}) \in \{+1, -1\}, \tag{4}$$

with

$$\Delta_{k,1} = \varepsilon_{5/2}(k) - \varepsilon_{3/2}(k), \tag{5}$$

where $\varepsilon_i(k)$ ($i = 5/2$ or $3/2$, and $k = \Gamma, A$) denotes the energy of the E_i band at point k. Evidently, $\zeta_1 = -1$ corresponds to the nontrivial case with band inversion, leading to the D_1 Dirac point. Similarly, ζ_2 is defined with $E_{5/2}$ replaced by $E_{1/2}$, and characterizes the band inversion between $E_{1/2}$ and $E_{3/2}$ bands for the formation of D_2. The nontriviality of ζ_i ($i = 1,2$) is accidental, depending on the material. For example, in CaAgAs, which is isostructural to CaAgBi, we find that $\zeta_1 = +1$ (see Fig. 6), indicating that the band inversion between $E_{3/2}$ and $E_{5/2}$ is removed. Therefore, D_1 point is eliminated.

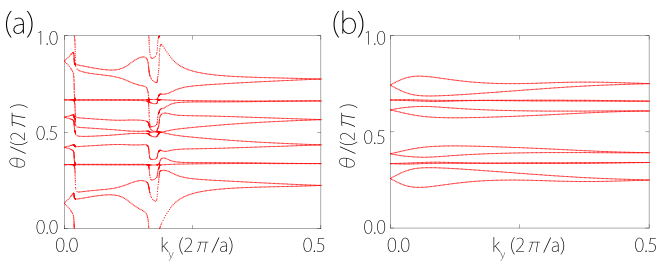

FIG. 5. The Wannier function center evolution for CaAgBi on the following planes in the Brillouin zone: (a) $k_z = 0$ and (b) $k_z = \pi$.

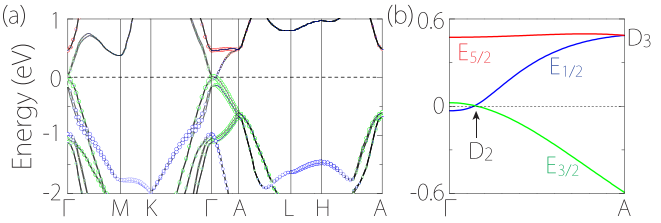

FIG. 6. (a) Band structure of CaAgAs (SOC included). The colored circles indicate the weight of orbital projection onto Ag-s (red), As-$p_{x/y}$ (green), and As-p_z (blue) orbitals. (b) Enlarged low-energy band structure along Γ-A.

Meanwhile, ζ_2 remains -1, so D_2 is kept, but it may ultimately be eliminated by a symmetry-preserving strain. In contrast, D_3 is invariably present in all these cases, since it is only determined by symmetry.

As mentioned, there exist a large family of ternary compounds with stuffed wurtzite structure [46,58,59]. Many members of this family share the same band features as discussed above (see Appendix A), exhibiting a hybrid Dirac semimetal phase with multiple Dirac points. Since the different kind of Dirac points are at different energies, it is possible to control the type of Dirac fermions in a single material by tuning the doping level, probing each kind separately. Alternatively, one may choose the proper material from the family which has the desired Dirac point closest to the Fermi level.

A salient feature of these materials is the broken inversion symmetry, which makes the Dirac bands completely split except along the k_z axis, leading to the birefringent Dirac fermions. This could give rise to a new double negative refraction effect at a p-n junction of such material. Consider the case when the Fermi level is most close to the D_1 point. Assume ballistic transport across a p-n junction along x direction, and we focus on the carrier dynamics in the x-y plane (the transverse momenta k_y and k_z are conserved). As illustrated in Fig. 7(a), with a constant k_z, there are two Fermi circles around the Dirac point, due to the band splitting.

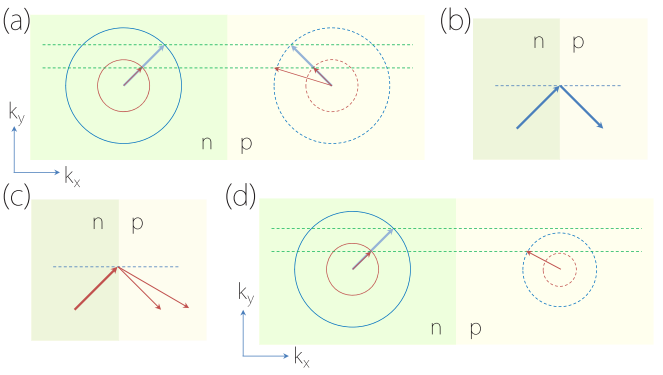

FIG. 7. Schematic figures showing Dirac fermion transport at a p-n junction along x. (a) Fermi circles (near D_1 point) for two sides of the junction. (b) Transmitted carriers show negative refraction at the interface. (c) Double refraction occurs for an incident state with two transmitted states [marked in (a)]. (d) At certain range of bias voltage and incident angle, only states from the inner Fermi circle get transmitted.

Carriers on each Fermi circle is chiral and undergo refractions at the junction interface, similar to that in graphene [60]. For *p-n* junction, this leads to negative refraction effect [Fig. 7(b)], and for incident state with two transmitted states, there are two negative refraction paths [see Fig. 7(c)]. In addition, by controlling the bias voltage and the incident angle of an incident electron beam, one can have transmission of carriers from only one of the Fermi circle [see Fig. 7(d)], whereas carriers from the other circle are totally reflected. This could be useful in electron optics to spatially separate the chiral carriers.

In conclusion, we have demonstrated a novel hybrid Dirac semimetal phase in CaAgBi-family materials. The low-energy band structure features three kinds of Dirac points: two pairs of accidental Dirac points with type-I and type-II dispersions, and a single essential Dirac point dictated by nonsymmorphic symmetry. We clarify their symmetry protections and characterize their individual low-energy Dirac fermions. Distinct from centrosymmetric Dirac semimetals, the Dirac bands here completely split due to the lack of inversion center. We show that this feature leads to interesting transport features at a *p-n* junction. We also find that different crystalline surfaces possess different topological surface states. The bulk Dirac points and the surface states can be experimentally probed by the angle-resolved photoemission spectroscopy (ARPES). Our findings make it possible to study multiple types of Dirac fermions and their interplays within a single material system.

ACKNOWLEDGMENTS

The authors thank H.-M. Guo and D. L. Deng for valuable discussion. C.C. and X.-L.S. acknowledge helpful discussion with Wei Li. This work is partly supported by the NSF of China (No. 11504013), and Singapore MOE Academic Research Fund Tier 2 (MOE2015-T2-2-144) and Tier 1 (SUTD-T1-2015004).

TABLE I. Character table for the three encountered representations of the C_{6v} double group.

C_{6v}	E	$2C_6$	$2C_3$	C_2	$3\sigma_d$	$3\sigma_v$
$E_{1/2}$	2	$\sqrt{3}$	1	0	0	0
$E_{3/2}$	2	0	-2	0	0	0
$E_{5/2}$	2	$-\sqrt{3}$	1	0	0	0

APPENDIX A: OTHER CANDIDATE MATERIALS IN THE FAMILY

Figure 8 show the band structures of some other members of the CaAgBi family: CaAuSb, CaAuBi, and SrAgBi. They also possess multiple kinds of Dirac points as discussed in the main text.

APPENDIX B: GROUP REPRESENTATIONS OF THREE LOW-ENERGY BANDS

As we have mentioned in Sec. IV, along the Γ-A path, each of the three low-energy bands are doubly degenerate (SOC included). They correspond to three distinct two-dimensional irreducible representations (IRs) of the C_{6v} double group, i.e., $E_{1/2}$, $E_{3/2}$, and $E_{5/2}$. Their symmetry properties can be inferred from the character table in Table I [61]. One can observe that the three IRs mainly differ in their behavior under C_6 operation. This can be understood by noticing that the C_6 double group alone possess three pairs of conjugated one-dimensional IRs (for angular momentum number $j = 1/2$, $3/2$, and $5/2$) [61]. With the inclusion of M_x, each conjugated pair will be bind together into a two-dimensional IR for the C_{6v} double group, hence leading to the three IRs encountered here.

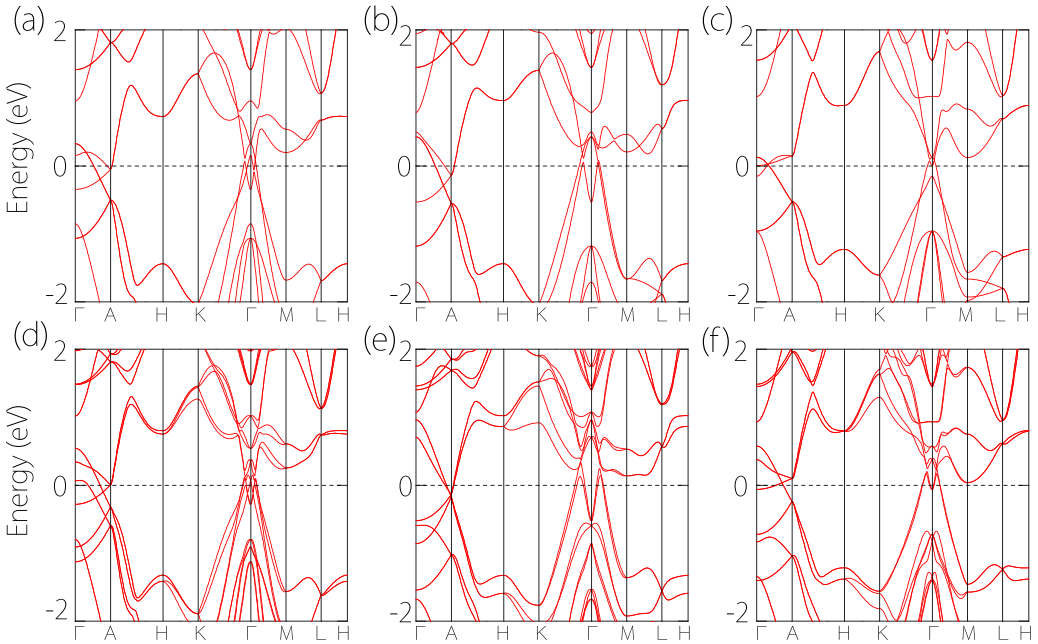

FIG. 8. Band structures of some other materials in CaAgBi family with the same crystal structure without (upper panels) and with (lower panes) SOC: (a) and (d) CaAuSb, (b) and (e) CaAuBi, and (c) and (f) SrAgBi.

APPENDIX C: DERIVATION OF MODEL EQ. (3)

The effective model around the essential Dirac point is constrained by the following symmetry operations in the little group at A point: the threefold rotation C_{3z}, the mirror plane M_x, the screw rotation S_{2z}, and the time reversal operation $\mathcal{T}$. Their matrix representations can be found in the standard reference [50] for space group No. 186, with

$$C_{3z} = \sigma_0\left(\frac{1}{2}\tau_0 + \frac{\sqrt{3}}{2}i\tau_y\right), \tag{C1}$$

$$M_x = i\sigma_0\tau_z, \tag{C2}$$

$$S_{2z} = \sigma_z\tau_y, \tag{C3}$$

$$\mathcal{T} = \sigma_x\tau_y K. \tag{C4}$$

Here σ_i and τ_i are the Pauli matrices, σ_0 and τ_0 are 2×2 identity matrix, and K is the complex conjugation operation. One verifies that these representations satisfy the required commutation relations between the symmetry operations. In the basis of this representation, we find that

$$\mathcal{H}_{D_3}(\boldsymbol{q}) = v_\perp\sigma_0\tau_z q_x - v_\perp\sigma_0\tau_x q_y + v_z\sigma_z\tau_0 q_z, \tag{C5}$$

where the wave-vector $\boldsymbol{q}$ is measured from A point. This is the model presented in Eq. (3). From this model, we obtain the energy eigenvalues with

$$E(\boldsymbol{q}) = \pm v_z q_z \pm v_\perp\sqrt{q_x^2 + q_y^2}, \tag{C6}$$

which is used to fit the DFT band structure around A point.

[1] C.-K. Chiu, J. C. Y. Teo, A. P. Schnyder, and S. Ryu, Rev. Mod. Phys. **88**, 035005 (2016).
[2] X. Dai, Nat. Phys. **12**, 727 (2016).
[3] Y. X. Zhao and Z. D. Wang, Phys. Rev. Lett. **110**, 240404 (2013).
[4] S. A. Yang, SPIN **06**, 1640003 (2016).
[5] X. Wan, A. M. Turner, A. Vishwanath, and S. Y. Savrasov, Phys. Rev. B **83**, 205101 (2011).
[6] S. Murakami, New J. Phys. **9**, 356 (2007).
[7] A. A. Burkov and L. Balents, Phys. Rev. Lett. **107**, 127205 (2011).
[8] H. Weng, C. Fang, Z. Fang, B. A. Bernevig, and X. Dai, Phys. Rev. X **5**, 011029 (2015).
[9] S.-M. Huang, S.-Y. Xu, I. Belopolski, C.-C. Lee, G. Chang, B. Wang, N. Alidoust, G. Bian, M. Neupane, C. Zhang *et al.*, Nat. Commun. **6**, 7373 (2015).
[10] B. Q. Lv, H. M. Weng, B. B. Fu, X. P. Wang, H. Miao, J. Ma, P. Richard, X. C. Huang, L. X. Zhao, G. F. Chen *et al.*, Phys. Rev. X **5**, 031013 (2015).
[11] S.-Y. Xu, I. Belopolski, N. Alidoust, M. Neupane, G. Bian, C. Zhang, R. Sankar, G. Chang, Z. Yuan, C.-C. Lee *et al.*, Science **349**, 613 (2015).
[12] G. E. Volovik, *The Universe in a Helium Droplet* (Clarendon, Oxford, 2003).
[13] H. Nielsen and M. Ninomiya, Phys. Lett. B **130**, 389 (1983).
[14] S. M. Young, S. Zaheer, J. C. Y. Teo, C. L. Kane, E. J. Mele, and A. M. Rappe, Phys. Rev. Lett. **108**, 140405 (2012).
[15] B.-J. Yang and N. Nagaosa, Nat. Commun. **5**, 4898 (2014).
[16] Z. Wang, Y. Sun, X.-Q. Chen, C. Franchini, G. Xu, H. Weng, X. Dai, and Z. Fang, Phys. Rev. B **85**, 195320 (2012).
[17] Z. K. Liu, B. Zhou, Y. Zhang, Z. J. Wang, H. M. Weng, D. Prabhakaran, S.-K. Mo, Z. X. Shen, Z. Fang, X. Dai *et al.*, Science **343**, 864 (2014).
[18] Z. Wang, H. Weng, Q. Wu, X. Dai, and Z. Fang, Phys. Rev. B **88**, 125427 (2013).
[19] Z. K. Liu, J. Jiang, B. Zhou, Z. J. Wang, Y. Zhang, H. M. Weng, D. Prabhakaran, S.-K. Mo, H. Peng, P. Dudin *et al.*, Nat. Mater. **13**, 677 (2014).
[20] M. Neupane, S.-Y. Xu, R. Sankar, N. Alidoust, G. Bian, C. Liu, I. Belopolski, T.-R. Chang, H.-T. Jeng, H. Lin *et al.*, Nat. Commun. **5**, 3786 (2014).
[21] S. Borisenko, Q. Gibson, D. Evtushinsky, V. Zabolotnyy, B. Büchner, and R. J. Cava, Phys. Rev. Lett. **113**, 027603 (2014).
[22] J. A. Steinberg, S. M. Young, S. Zaheer, C. L. Kane, E. J. Mele, and A. M. Rappe, Phys. Rev. Lett. **112**, 036403 (2014).
[23] A. A. Soluyanov, D. Gresch, Z. Wang, Q. Wu, M. Troyer, X. Dai, and B. A. Bernevig, Nature (London) **527**, 495 (2015).
[24] Y. Xu, F. Zhang, and C. Zhang, Phys. Rev. Lett. **115**, 265304 (2015).
[25] T.-R. Chang, S.-Y. Xu, D. S. Sanchez, W.-F. Tsai, S.-M. Huang, G. Chang, C.-H. Hsu, G. Bian, I. Belopolski, Z.-M. Yu *et al.*, Phys. Rev. Lett. **119**, 026404 (2017).
[26] F. Fei, X. Bo, R. Wang, B. Wu, J. Jiang, D. Fu, M. Gao, H. Zheng, Y. Chen, F. Song *et al.*, Phys. Rev. B **96**, 041201 (2017).
[27] R. C. Xiao, P. L. Gong, Q. S. Wu, W. J. Lu, M. J. Wei, J. Y. Li, H. Y. Lv, X. Luo, P. Tong, X. B. Zhu *et al.*, Phys. Rev. B **96**, 075101 (2017).
[28] H.-J. Noh, J. Jeong, E.-J. Cho, K. Kim, B. I. Min, and B.-G. Park, Phys. Rev. Lett. **119**, 016401 (2017).
[29] K. Zhang, M. Yan, H. Zhang, H. Huang, M. Arita, Z. Sun, W. Duan, Y. Wu, and S. Zhou, Phys. Rev. B (to be published) [arXiv:1703.04242].
[30] H. Huang, S. Zhou, and W. Duan, Phys. Rev. B **94**, 121117 (2016).
[31] M. Yan, H. Huang, K. Zhang, E. Wang, W. Yao, K. Deng, G. Wan, H. Zhang, M. Arita, H. Yang *et al.*, Nat. Commun. **8**, 257 (2017).
[32] P.-J. Guo, H.-C. Yang, K. Liu, and Z.-Y. Lu, Phys. Rev. B **95**, 155112 (2017).
[33] C. Le, S. Qin, X. Wu, X. Dai, P. Fu, and J. Hu, arXiv:1606.05042.
[34] H.-X. Wang, Y. Chen, Z. H. Hang, H.-Y. Kee, and J.-H. Jiang, arXiv:1703.09899.
[35] Z.-M. Yu, Y. Yao, and S. A. Yang, Phys. Rev. Lett. **117**, 077202 (2016).
[36] S. Tchoumakov, M. Civelli, and M. O. Goerbig, Phys. Rev. Lett. **117**, 086402 (2016).
[37] S. Guan, Z.-M. Yu, Y. Liu, G.-B. Liu, L. Dong, Y. Lu, Y. Yao, and S. A. Yang, npj Quantum Mater. **2**, 23 (2017).
[38] F.-Y. Li, X. Luo, X. Dai, Y. Yu, F. Zhang, and G. Chen, Phys. Rev. B **94**, 121105 (2016).
[39] X. Kong, J. He, Y. Liang, and S.-P. Kou, Phys. Rev. A **95**, 033629 (2017).

[40] G. Kresse and J. Furthmüller, Phys. Rev. B **54**, 11169 (1996).
[41] G. Kresse and D. Joubert, Phys. Rev. B **59**, 1758 (1999).
[42] P. E. Blöchl, Phys. Rev. B **50**, 17953 (1994).
[43] J. P. Perdew, K. Burke, and M. Ernzerhof, Phys. Rev. Lett. **77**, 3865 (1996).
[44] H. J. Monkhorst and J. D. Pack, Phys. Rev. B **13**, 5188 (1976).
[45] A. A. Mostofi, J. R. Yates, G. Pizzi, Y.-S. Lee, I. Souza, D. Vanderbilt, and N. Marzari, Comput. Phys. Commun. **185**, 2309 (2014).
[46] Z.-M. Sun, J.-Y. Xie, D.-C. Pan, and J.-G. Mao, J. Alloys Compd. **430**, 71 (2007).
[47] M. P. Kennett, N. Komeilizadeh, K. Kaveh, and P. M. Smith, Phys. Rev. A **83**, 053636 (2011).
[48] B. Roy, P. M. Smith, and M. P. Kennett, Phys. Rev. B **85**, 235119 (2012).
[49] N. Komeilizadeh and M. P. Kennett, Phys. Rev. B **90**, 045131 (2014).
[50] C. J. Bradley and A. P. Cracknell, *The Mathematical Theory of Symmetry in Solids* (Clarendon, Oxford, 1972).
[51] X.-L. Sheng, Z. Wang, R. Yu, H. Weng, Z. Fang, and X. Dai, Phys. Rev. B **90**, 245308 (2014).
[52] X.-L. Sheng, Z.-M. Yu, R. Yu, H. Weng, and S. A. Yang, J. Phys. Chem. Lett. **8**, 3506 (2017).
[53] L. Fu and C. L. Kane, Phys. Rev. B **76**, 045302 (2007).
[54] R. Yu, X. L. Qi, A. Bernevig, Z. Fang, and X. Dai, Phys. Rev. B **84**, 075119 (2011).
[55] A. A. Soluyanov and D. Vanderbilt, Phys. Rev. B **83**, 035108 (2011).
[56] Q. Wu, S. Zhang, H.-F. Song, M. Troyer, and A. A. Soluyanov, arXiv:1703.07789.
[57] X.-L. Sheng and B. K. Nikolić, Phys. Rev. B **95**, 201402 (2017).
[58] A. Yamakage, Y. Yamakawa, Y. Tanaka, and Y. Okamoto, J. Phys. Soc. Jpn. **85**, 013708 (2016).
[59] Y. Okamoto, T. Inohara, A. Yamakage, Y. Yamakawa, and K. Takenaka, J. Phys. Soc. Jpn. **85**, 123701 (2016).
[60] V. V. Cheianov, V. Fal'ko, and B. L. Altshuler, Science **315**, 1252 (2007).
[61] P. Jacobs, *Group Theory with Applications in Chemical Physics* (Cambridge University Press, Cambridge, 2005).